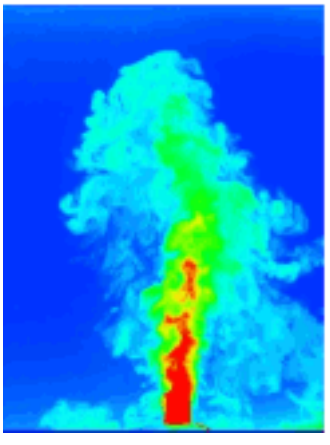

Journal of Turbulence
Publication details, including instructions for authors and subscription information:
http://www.tandfonline.com/loi/tjot20

Effect of wall temperature on hypersonic turbulent boundary layer

You-Biao Chu[ab], Yue-Qing Zhuang[a] & Xi-Yun Lu[a]

[a] Department of Modern Mechanics, University of Science and Technology of China, Hefei, Anhui, China

[b] The National Key Laboratory of Combustion, Thermostructure and Flow of SRM, The 41st Institute of the Fourth Academy of CASC, Xi'an, China

Published online: 18 Dec 2013.

To cite this article: You-Biao Chu, Yue-Qing Zhuang & Xi-Yun Lu (2013) Effect of wall temperature on hypersonic turbulent boundary layer, Journal of Turbulence, 14:12, 37-57, DOI: 10.1080/14685248.2013.867348

To link to this article: http://dx.doi.org/10.1080/14685248.2013.867348

Journal of Turbulence, 2013
Vol. 14, No. 12, 37–57, http://dx.doi.org/10.1080/14685248.2013.867348

Effect of wall temperature on hypersonic turbulent boundary layer

You-Biao Chu[a,b], Yue-Qing Zhuang[a] and Xi-Yun Lu[a]*

[a]*Department of Modern Mechanics, University of Science and Technology of China, Hefei, Anhui, China;* [b]*The National Key Laboratory of Combustion, Thermostructure and Flow of SRM, The 41st Institute of the Fourth Academy of CASC, Xi'an, China*

(*Received 26 July 2013; accepted 14 November 2013*)

Turbulent boundary layers at Mach 4.9 with the ratio of wall temperature to recovery temperature from 0.5 to 1.5 are investigated by means of direct numerical simulation. Various fundamental properties relevant to the influence of wall temperature on Morkovin's scaling, standard and modified strong Reynolds analogies, and coherent vortical structures have been studied. It is identified that the scaling relations proposed for cool and adiabatic wall conditions, such as Morkovin's scaling and the modified strong Reynolds analogy, are also applicable for hot wall condition. Moreover, the relation between the density and temperature fluctuations under the second-order approximation is derived and verified to provide a reliable prediction. Based on the analysis of coherent vortical structures, it is found that the orientation of vortex core can be quantitatively determined by means of the vector with its direction and modulus using the local strain direction and the imaginary part of the eigenvalue of velocity gradient tensor, respectively. As the increase of wall temperature, the spanwise distance between the two legs of hairpin vortex increases, and the mean swirling strength and the angle of vortical structure with respect to the wall plane also increase in the inner layer. The statistical properties relevant to vortical structures are nearly insensitive to the wall temperature in the outer layer.

Keywords: compressible flow; turbulent boundary layer

1. Introduction

Both supersonic and hypersonic turbulent boundary layers occur usually in high-speed vehicles and also involve the fundamental challenges in fluid mechanics. One of the important differences between them is the wall temperature conditions [1]. For a flight vehicle at supersonic speeds, the surface temperature is essentially adiabatic, while for a flight vehicle at hypersonic speeds, the surface temperature is significantly lower than the adiabatic wall temperature (i.e. cool wall) due to considerable radiative cooling and internal heat transfer. Moreover, in the propulsion systems, the surface temperature is significantly larger than the adiabatic wall temperature (i.e. hot wall) due to the combustion of propellant. Thus, various fundamental mechanisms dictating the flow characteristics of hypersonic turbulent boundary layers are still of great interest for future detailed studies.

For compressible turbulent boundary layers, Morkovin's hypothesis [2] is one of the most important scaling laws, which indicates that the differences from incompressible turbulence can be predicted by the mean variations of fluid properties for moderate free-stream Mach numbers about less than 5. The essential dynamics of supersonic turbulent boundary

*Corresponding author. Email: xlu@ustc.edu.cn

layers closely resemble incompressible ones based on experimental measurement [3] and numerical simulation [4,5]. The other important relationship in the analysis of compressible turbulent boundary layer is the strong Reynolds analogy (SRA), which connects temperature fluctuation to streamwise velocity fluctuation and is used to extend incompressible turbulence models to compressible flows. Even though the validity of Morkovin's hypothesis as well as the standard and modified SRA has been assessed through a wide range of wall temperatures [1], free-stream Mach numbers [6,7] and enthalphy conditions [8], equivalent information is not yet known for the hot wall.

The coherent vortical structures play an important role in turbulent boundary layers [9]. Theodorsen [10] first proposed that incompressible turbulent boundary layers are populated by horseshoe-shaped vortices or hairpin-like structures attached to the wall, which can be described as a pair of counter-rotating quasi-streamwise vortices near the wall. He also postulated that horseshoe-shaped vortices incline along the principal extensive strain direction by an angle of 45° with respect to the wall. Head and Bandyopadhyay [11] also experimentally confirmed the structural features in terms of the flow visualisation of individual hairpin vortices. Ong and Wallace [12] then achieved the similar results from the analysis of the covariance integrands of the vorticity components in the streamwise and wall-normal planes. Typically, Ganapathisubramani et al. [13] studied the geometric orientation of vortex cores in the logarithmic layer and in the wake region using dual-plane particle image velocimetry. They noticed that the most probable elevation, represented by the angle formed by the vortex core with respect to the wall plane, is about 38° in the logarithmic layer and 33° in the wake region, and the most probable eddy inclination angle, represented by the angle taken in the streamwise–wall-normal plane, is approximately 45° in both the regions. Even though the structural features of incompressible boundary layers seem to be well understood, the relevant behaviours of compressible counterparts are much less known.

The dynamics of coherent vortical structures of supersonic boundary layers have been recognised to be important. The relevant experimental investigations are still scarce because of the limitation of measurement techniques. Some available supersonic experimental data indicated little influence of compressibility on the statistical properties of coherent vortical structures [14]. Pirozzoli et al. [15] quantitatively analysed coherent vortical structures in supersonic boundary layer at Mach 2 by means of a spatial direct numerical simulation (DNS). They predicted structural similarities with the incompressible case. In particular, the inner layer including the viscous sublayer and the buffer layer is mostly populated by quasi-streamwise vortices inclined at 10° with respect to the wall, and the outer layer including the logarithmic layer and the wake region is populated by a large variety of structures including hairpin vortices and hairpin packets. Wang and Lu [16] investigated the inclination angles of coherent vortical structures in supersonic turbulent boundary layer at Mach 2 by means of statistical analysis of the covariance integrand of two vorticity components, and noticed that the results obtained are similar to the incompressible case. To our knowledge, however, the relevant study of the effect of wall temperature on the orientation of vortical structures in compressible turbulent boundary layer has never been performed.

In the present study, the statistical properties of compressible turbulent boundary layers under isothermal-wall conditions are investigated by means of DNS at Mach number $M_\delta = 4.9$. The purpose of this study is to achieve an improved understanding of some of the fundamental properties relevant to the influence of wall temperature on Morkovin's scaling, standard and modified SRA relations, and coherent vortical structures.

This paper is organised as follows. The flow conditions and simulation details are presented in Section 2. The results and the relevant validations are then given in Section 3, and concluding remarks in Section 4.

2. Simulation details

2.1. *Simulation method*

The numerical treatment is briefly described here. The three-dimensional compressible Navier–Stokes equations are employed. To non-dimensionalise the equations, we use the boundary layer edge variables including the density ρ_δ, temperature T_δ, speed of sound c_δ, and the boundary layer thickness at the inlet δ_0 as characteristic quantities. The equations are numerically solved by a seventh-order weighted essentially non-oscillatory scheme for the convective terms [17] and a sixth-order central difference scheme for the viscous terms. The temporal integration is performed using a fourth-order Runge–Kutta algorithm [18]. The relevant numerical strategy has been verified to be reliable in the simulation of compressible turbulent boundary layers [19,20]. Moreover, we should indicate that recent developments in numerical algorithms have also shown that compressible computations can be performed using central, non-dissipative scheme, which are inherently superior to upwind schemes [21,22].

The initial and boundary conditions are presented as follows. A compressible turbulent boundary layer obtained in our previous work [19] is employed to initialise the present simulation by means of initialisation procedures given by Martín [23]. The inflow boundary condition is treated using the rescaling method proposed by Xu and Martín [24]. Periodic conditions are used in the spanwise direction to exploit homogeneity. No-slip condition is applied on the wall. The wall temperature is prescribed for three typical cases given below in detail. A sponge layer is placed before the outlet boundary where the variables are extrapolated from the interior [25]. In order to minimise the reflection of small disturbances back into the computational domain, non-reflecting boundary conditions are specified at the upper boundary.

2.2. *Flow conditions*

To study the effect of wall temperature, we consider compressible turbulent boundary layers with free-stream Mach number $M_\delta = 4.9$ and wall-to-recovery temperature ratio T_w/T_r ranging from 0.5 to 1.5, where $T_r \equiv T_\delta\left(1 + r((\gamma - 1)/2)M_\delta^2\right)$ with $r = 0.89$. Table 1 lists the boundary layer properties at the inlet for three typical cases after the initial transient, providing wall temperature T_w/T_δ and different definitions of Reynolds number, where $\mathrm{Re}_{\delta_2} \equiv \rho_\delta u_\delta \theta/\mu_w$, $\mathrm{Re}_\theta \equiv \rho_\delta u_\delta \theta/\mu_\delta$, $\mathrm{Re}_\tau \equiv \rho_w u_\tau \delta/\mu_w$, and $\mathrm{Re} \equiv \rho_\delta u_\delta \delta/\mu_\delta$. The subscripts δ and w denote quantities at the boundary layer edge and at the wall, respectively.

Table 1. Boundary layer properties at the inlet for the DNS cases.

Case	M_δ	T_w/T_r	T_w/T_δ	Re_{δ_2}	Re_θ	Re_τ	Re
M5T2	4.9	0.5	2.62	1817	3480	532	0.58×10^5
M5T5	4.9	1.0	5.25	1826	5559	397	1.09×10^5
M5T8	4.9	1.5	7.91	1903	7612	353	1.73×10^5

Table 2. Grid resolution and domain size for the DNS cases.

Case	L_x/δ_0	L_y/δ_0	L_z/δ_0	N_x	N_y	N_z	Δx^+	Δy^+	Δz_w^+
M5T2	20	3	12	1400	360	256	7.6	4.4	0.87
M5T5	20	3	12	1024	256	256	7.7	4.6	0.78
M5T8	20	3	12	1024	256	256	6.8	4.1	0.81

Following the approach of Duan, Beekman, and Martín [1], we here match Re_{δ_2} for different wall-temperature cases in order to keep wall temperature as the only scaling parameter. According to the wall temperature, M5T2 and M5T8 are referred to be as the cool and the hot wall conditions, respectively. The wall temperature for M5T5 is prescribed to be nearly the recovery temperature T_r; therefore, M5T5 is referred to be as the adiabatic wall condition.

2.3. *Simulation parameters*

The computational domain size and grid resolution have been carefully examined. The domain is chosen as $L_x \times L_y \times L_z = 20\delta_0 \times 3\delta_0 \times 12\delta_0$. The number of grid points ($N_x \times N_y \times N_z$) and the grid size ($\Delta x \times \Delta y \times \Delta z$) are given in Table 2, where x, y, and z represent the streamwise, spanwise, and wall-normal directions, respectively. The mesh is uniformly distributed in the streamwise and spanwise directions, and is stretched by a hyperbolic tangent mapping function in the wall-normal direction. The superscript + indicates scaling with wall values including the friction velocity $u_\tau = (\tau_w/\rho_w)^{1/2}$ and the viscous length scale $\delta_v = \nu_w/u_\tau$.

Further, to assess the adequacy of the domain size, Figure 1 typically shows the streamwise two-point correlations of the streamwise, spanwise, and wall-normal velocity fluctuations and of the density and temperature fluctuations for M5T5. It is identified that the correlations nearly vanish at larger separations, indicating that the domain length used in the present study is sufficient. Similar characters have also been obtained for the other two cases. Furthermore, the present simulation has been validated by comparing the calculated results with previous DNS data [6], which will be given in Section 3.1. Moreover, the present numerical strategy has already been validated for compressible turbulent boundary layers

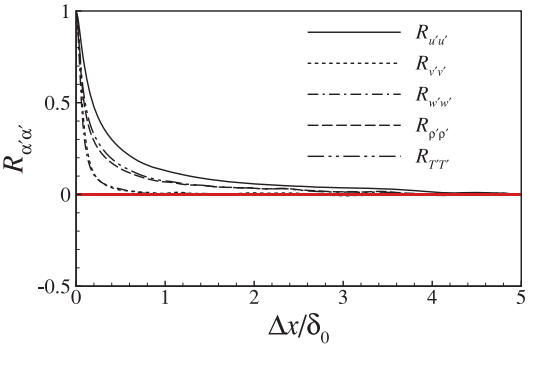

Figure 1. Two-point correlations $R_{\alpha'\alpha'}$ for the streamwise, spanwise, and wall-normal velocity components, density, and temperature at $z/\delta_0 = 0.1$ for M5T5.

in our recent papers [19,20]. We have carefully examined the physical model and numerical approach used in this study and have verified that the calculated results are reliable.

At the selected flow condition, a fully developed turbulent state is reached in the region of $5 < x/\delta_0 < 15$. In order to study the statistical properties of the turbulent boundary layer, we used 250 flow samples with equal intervals in time over approximately four non-dimensional time units (δ_0/c_δ) for each case. The samples are collected over a small portion of the boundary layer with $9 < x/\delta_0 < 11$. Because of the small variation of Reynolds number, the growth of the boundary layer is negligible and all statistical properties are regarded to be functions only of the wall-normal coordinate [15,19].

To clearly present the post-process, some symbols used in this paper are introduced as follows. The Reynolds average of a variable f in time and in space along the streamwise and spanwise directions is denoted by $\bar{f}$, and the corresponding fluctuation is defined as $f' = f - \bar{f}$. The Favre average is a density-weighted average $\tilde{f} = \overline{\rho f}/\bar{\rho}$. Then, the fluctuation about the Favre average is obtained as $f'' = f - \tilde{f}$.

3. Results and discussion

3.1. *Turbulence statistics*

The Morkovin's hypothesis, the relationship between the mean temperature and mean streamwise velocity, and the fluctuations of quantities have been investigated for adiabatic and cool wall conditions [1]. However, the relevant properties for hot wall condition are needed to be analysed and are assessed here based on the present DNS data.

3.1.1. *Mean flow*

The van Driest transformed velocity U^+_{VD} represents the density-weighted mean streamwise velocity and is described as

$$U^+_{\mathrm{VD}} = \int_0^{\bar{u}^+} (\bar{\rho}/\bar{\rho}_w)^{1/2} \mathrm{d}\bar{u}^+. \tag{1}$$

Figure 2 shows the van Driest transformed velocity. For comparison, the incompressible linear and logarithmic laws are also plotted and are represented as $U^+_{\mathrm{VD}} = z^+$ and $U^+_{\mathrm{VD}} = 1/\kappa \ln z^+ + C$, respectively, where $\kappa \approx 0.41$ and $C \approx 5.2$ [26]. The profiles for different wall-temperature conditions are essentially consistent with the incompressible linear scaling

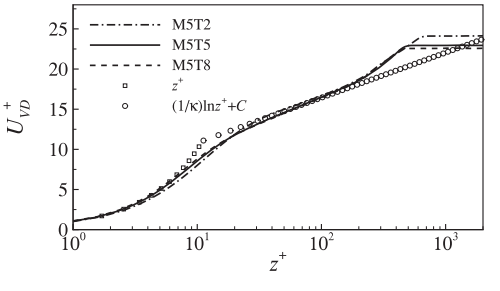

Figure 2. The van Driest transformed velocity with linear scaling and logarithmic scaling lines [26] for different wall-temperature conditions.

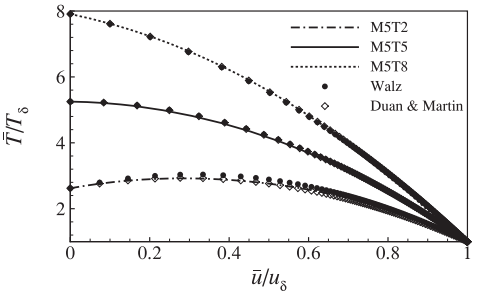

Figure 3. Test of modified Crocco relations for different wall-temperature cases.

and logarithmic scaling lines, even though the logarithmic region is narrow due to low-Reynolds-number flows. It is also observed that the additive constant C for the cooled wall case is slightly higher than the other two cases. Moreover, the region of linear viscous sublayer shrinks with the decrease of wall temperature, indicating that the influence of wall temperature mainly occurs in the near-wall region. The relevant phenomena are also consistent with the previous DNS results for adiabatic and cool wall conditions [1].

Further, we investigate the relation of the mean temperature and mean streamwise velocity. The modified Crocco relation by Walz [27] is commonly used to analyse the mean temperature and streamwise velocity in zero-pressure-gradient turbulent boundary layers, namely,

$$\frac{\bar{T}}{T_\delta} = \frac{T_w}{T_\delta} + \frac{T_r - T_w}{T_\delta}\left(\frac{\bar{u}}{u_\delta}\right) + \frac{T_\delta - T_r}{T_\delta}\left(\frac{\bar{u}}{u_\delta}\right)^2. \tag{2}$$

Then, Duan and Martín [8] proposed a generalised form of the modified Crocco relation,

$$\frac{\bar{T}}{T_\delta} = \frac{T_w}{T_\delta} + \frac{T_r - T_w}{T_\delta} f\left(\frac{\bar{u}}{u_\delta}\right) + \frac{T_\delta - T_r}{T_\delta}\left(\frac{\bar{u}}{u_\delta}\right)^2, \tag{3}$$

where $f(\bar{u}/u_\delta)$ is an empirical function based on the DNS data fitting and is given as [8] $f(\bar{u}/u_\delta) = 0.8259(\bar{u}/u_\delta) + 0.1741(\bar{u}/u_\delta)^2$.

Figure 3 shows the comparison between the modified Crocco relations and DNS results. It is seen that an agreement of the present DNS result and the prediction using Equations (2) and (3) occurs for the adiabatic and hot wall conditions. The deviation of the data obtained by Equation (2) from the DNS result is obvious with the largest discrepancy about 5% for the cool wall condition, and an improved prediction is obtained by Equation (3). According to the profiles in Figure 3, it is identified that the relations of Equations (2) and (3) are reasonably applicable for hot wall condition.

3.1.2. *Turbulence quantities*

The effect of wall temperature on turbulence intensities and thermodynamic quantities fluctuations is investigated. Figure 4 shows the turbulence intensities and density-weighted intensities in the streamwise, spanwise, and wall-normal directions across the boundary layer for different wall-temperature conditions. As a typical validation, it is seen that the present results agree well with the previous DNS data of Duan et al. [6] for an adiabatic

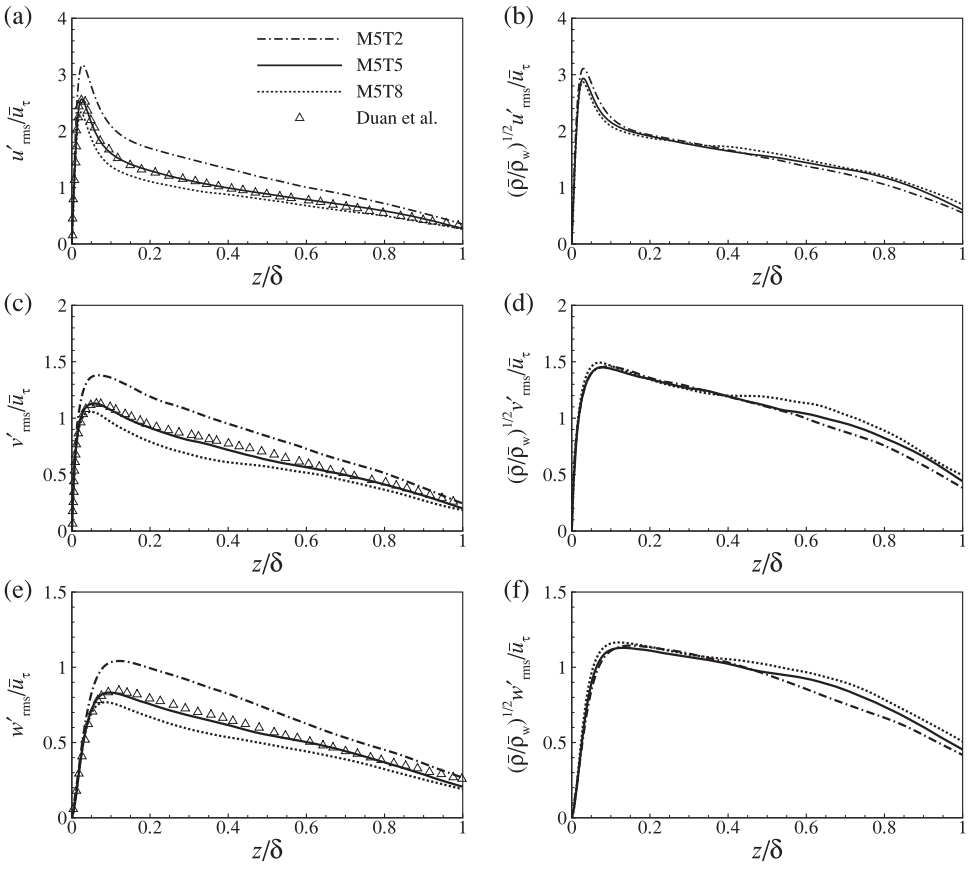

Figure 4. Turbulence intensities and density-weighted turbulence intensities of the (a,b) streamwise, (c,d) spanwise, and (e,f) wall-normal fluctuating velocity components for different wall-temperature conditions. Symbols denote the DNS data of Duan et al. [6] for an adiabatic turbulent boundary layer at $M_\delta = 4.9$ and $\mathrm{Re}_{\delta 2} = 1578$.

turbulent boundary layer at $M_\delta = 4.9$ and $\mathrm{Re}_{\delta 2} = 1578$. Then, by Morkovin's scaling which takes into account the variation of the mean flow properties, the profiles of the density-weighted intensities collapse together for different wall-temperature conditions, especially for $z/\delta < 0.4$. Moreover, the turbulence intensity in the streamwise is significantly stronger than the ones in the spanwise and wall-normal directions. The turbulence intensities in all the directions are weakened with the increase of wall temperature.

The fluctuations of thermodynamic quantities are shown in Figures 5 and 6. For comparison, the present results agree with the DNS data [6]. As shown in Figure 5, for the root-mean-square (rms) value of pressure fluctuation normalised by $\bar{p}_w$ and $\bar{\rho}_w \bar{u}_\tau^2$, the magnitude of pressure fluctuation normalised by $\bar{p}_w$ decreases obviously with the increase of wall temperature. A better collapse of the profiles is achieved when p'_{rms} is normalised by $\bar{\rho}_w \bar{u}_\tau^2$, especially for $z/\delta < 0.4$. Figure 6 shows the rms values of density and temperature fluctuations normalised by the corresponding mean values. Opposite to the pressure fluctuation, a significant increase is observed in the magnitudes of density and temperature fluctuations as the wall temperature increases.

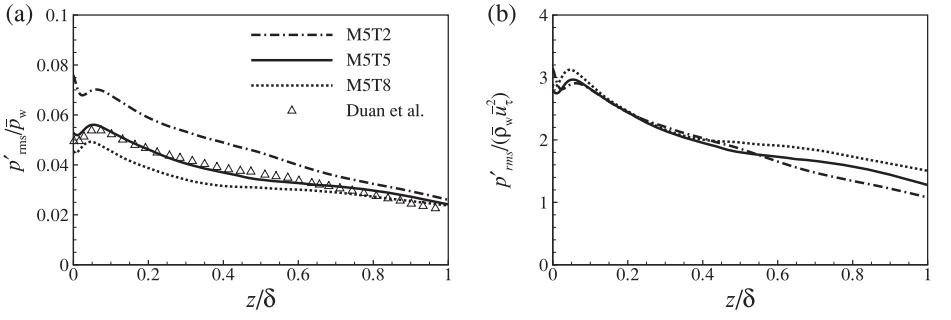

Figure 5. Profiles of $p'_{\rm rms}$ versus z/δ, scaled by (a) $\bar{p}_w$ and (b) $\bar{\rho}_w\bar{u}_\tau^2$.

A density fluctuation is usually estimated using the first-order approximation and assuming that the pressure fluctuation is negligible in a turbulent boundary layer [23]. Then, a relation reaches

$$\frac{\rho'}{\bar{\rho}} = -\frac{T'}{\bar{T}}. \tag{4}$$

In this study, we further use a second-order approximation to derive the relation. Then, the equation of state under the second-order approximation is expressed as

$$\frac{p'}{\bar{p}} = \frac{\rho'}{\bar{\rho}} + \frac{T'}{\bar{T}} + \left(\frac{\rho'}{\bar{\rho}}\right)\left(\frac{T'}{\bar{T}}\right). \tag{5}$$

By neglecting the pressure fluctuation, we obtain the relation between the density and temperature fluctuations:

$$\frac{\rho'}{\bar{\rho}} = \frac{-T'/\bar{T}}{1 + T'/\bar{T}}. \tag{6}$$

Figure 7 shows the joint probability density functions (PDFs) of temperature fluctuation $(T'/\bar{T})$ and density fluctuation $(\rho'/\bar{\rho})$ at $z^+ = 15$ and $z/\delta = 0.5$. The conditional average values of density fluctuation $\langle\rho'/\bar{\rho}|T'/\bar{T}\rangle$ are drawn by red lines. The first- and second-order

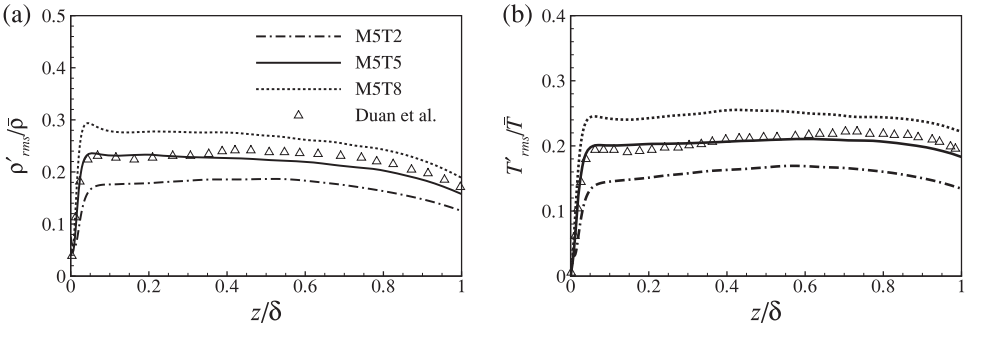

Figure 6. Profiles of (a) $\rho'_{\rm rms}/\bar{\rho}$ and (b) $T'_{\rm rms}/\bar{T}$ versus z/δ for different wall-temperature conditions.

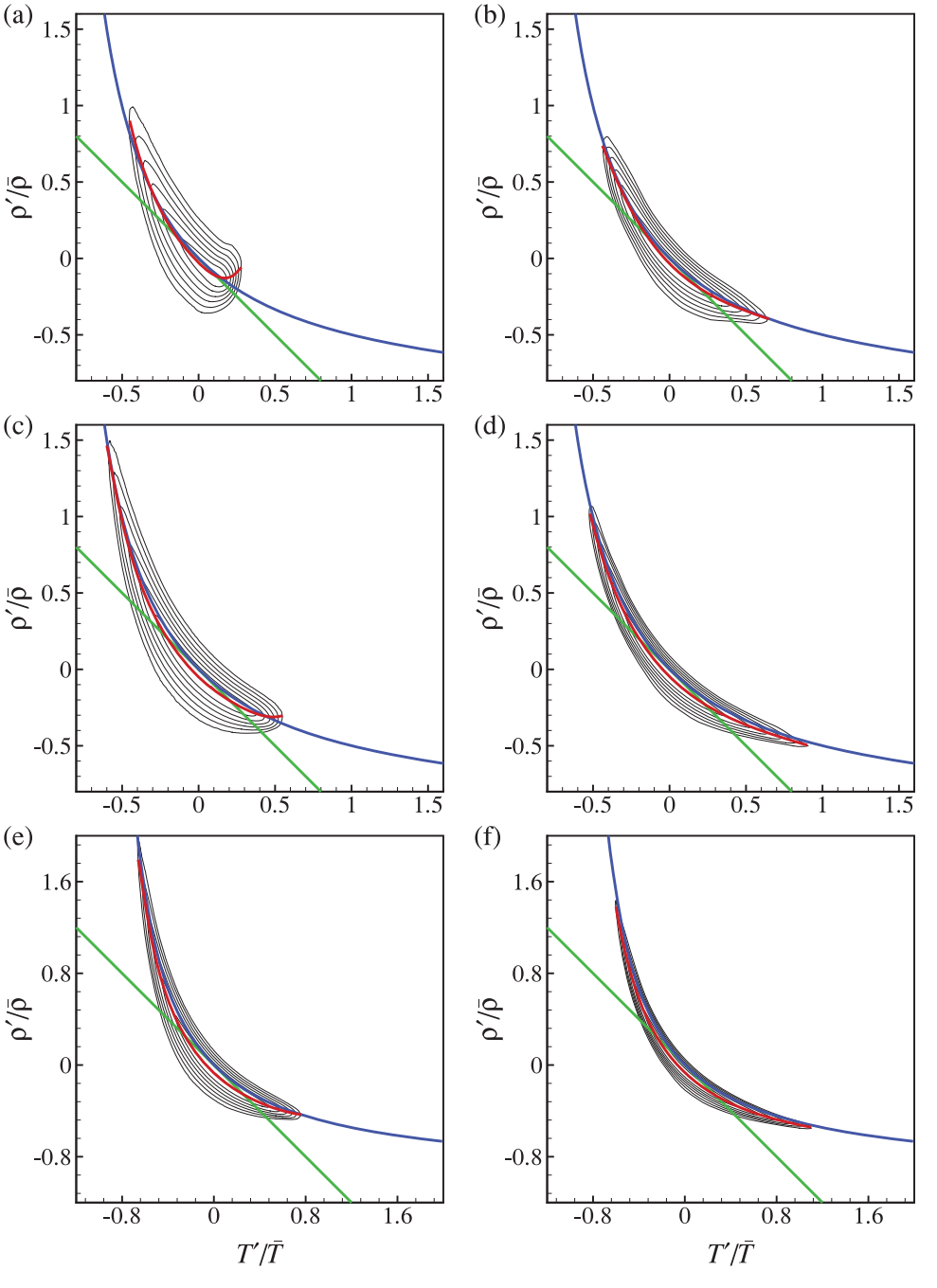

Figure 7. Joint PDFs of $T'/\bar{T}$ and $\rho'/\bar{\rho}$ on a logarithmic scale for (a,b) M5T2, (c,d) M5T5, and (e,f) M5T8. Left column for $z^+ = 15$, right column for $z/\delta = 0.5$. The outer contour level is -3 and the inner contour level is 0. The increment of contours is 0.5. The red, green, and blue lines are given by $\langle \rho'/\bar{\rho} | T'/\bar{T} \rangle$, Equations (4), and (6), respectively.

approximations are denoted by green and blue lines, respectively. It is seen that for the two wall-normal locations, the discrepancy between Equation (4) and DNS results significantly increases as the temperature fluctuation increases. However, an excellent agreement of Equation (6) with the conditional average values of density fluctuation is obtained, except for the range of $T' > 0$ in Figure 7(a) which shows the results at $z^+ = 15$ for M5T2. Therefore, the second-order approximation developed in this study demonstrates a better prediction with respect to the first-order approximation.

Furthermore, the small deviation of Equation (6) and DNS results is associated with neglecting the pressure fluctuation in the proceeding derivation. It is seen from Figure 5(a) that, with the increase of wall temperature and distance away from the wall, the normalised pressure fluctuation decreases; thus, fluid particles are more clustered near the blue lines which denote the second-order approximation. This behaviour is also confirmed by the results of the outer layer for the hot wall condition as shown in Figure 7(f), where the contours of the joint PDFs mostly lie near the blue line. Therefore, Equation (6) can be applied to make a more reliable prediction of the relation between density and temperature fluctuations in compressible turbulent boundary layers.

3.2. *Reynolds analogies*

The Reynolds analogies and the relevant properties are further investigated for different wall conditions. Morkovin [2] proposed five SRA relations. We will mainly analyse three typical ones in this study. One relation of them is described as

$$\frac{T''_{\mathrm{rms}}/\tilde{T}}{(\gamma-1)M^2(u''_{\mathrm{rms}}/\tilde{u})} \approx 1, \tag{7}$$

with $M^2 \equiv \tilde{u}^2/\gamma R\tilde{T}$.

Figure 8 shows the profiles using Equation (7). It is seen that the profile is around unity over $z/\delta > 0.02$ only for adiabatic wall condition (i.e. M5T5). The left-hand side of Equation (7) increases with the increase of wall temperature. Accounting for the influence of heat flux, Huang et al. [28] proposed a modified Reynolds analogy (HSRA), which is

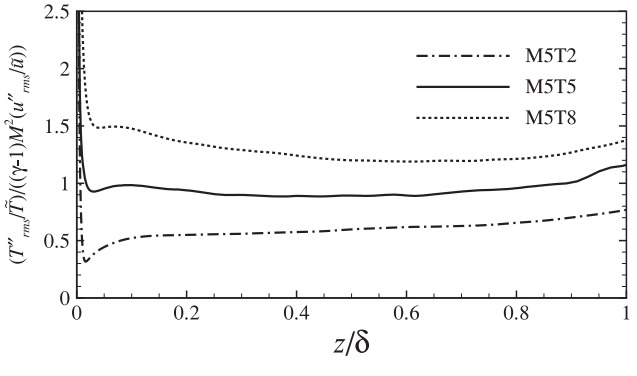

Figure 8. Plot of the strong Reynolds analogy expressed by Equation (7) for different wall-temperature conditions.

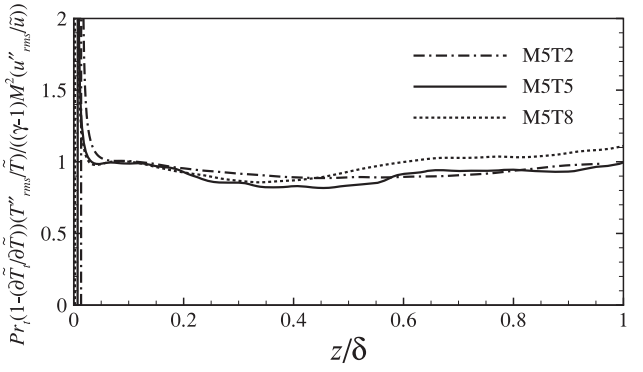

Figure 9. Plot of modified strong Reynolds analogy by Huang et al. [28], as expressed by Equation (8), for different wall-temperature conditions.

given by

$$\frac{T''_{\rm rms}/\tilde{T}}{(\gamma-1)M^2(u''_{\rm rms}/\tilde{u})} \approx \frac{1}{{\rm Pr}_t(1-(\partial\tilde{T}_t/\partial\tilde{T}))}, \tag{8}$$

where T_t is the total temperature and ${\rm Pr}_t$ is the turbulent Prandtl number. It has been verified that HSRA performs well for turbulent boundary layers with both adiabatic and cool wall conditions [1,4,6,29]. This behaviour is also confirmed from the profiles predicted by Equation (8) in Figure 9. Moreover, it is also determined that the relation (8) is reliably applicable for hot wall condition except the near-wall region and removes the wall-temperature dependence of Equation (7).

Another SRA relation is related to the turbulent Prandtl number which is given as [2]

$${\rm Pr}_t = \frac{\overline{\rho u'' w''}(\partial\tilde{T}/\partial z)}{\overline{\rho w'' T''}(\partial\tilde{u}/\partial z)} \approx 1. \tag{9}$$

Then, Figure 10 plots the turbulent Prandtl number across the boundary layer. It is seen that ${\rm Pr}_t$ is essentially around unity in the boundary layer with a gradual decrease versus the normal-wall distance and seems insensitive to the wall conditions considered here.

Further, the correlation between temperature and velocity fluctuations is also the SRA relation, that is,

$$-R_{u''T''} \approx 1. \tag{10}$$

Then, Figure 11 shows this correlation across the boundary layer. It is seen that u'' and T'' are not perfectly anti-correlated and $-R_{u''T''}$ is around 0.6 in the outer part of the boundary layer for all the three wall conditions, consistent with the results reported by Duan et al. [1] for the adiabatic and cool cases. Moreover, the positive correlation occurs in a region close to the wall for the cool case. This behaviour is associated with the local mean temperature gradient [1] and is also noticed in cooled-wall flows [1,30].

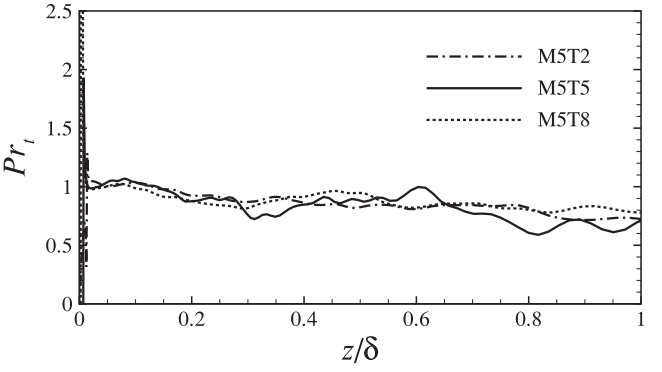

Figure 10. Plot of Pr_t for different wall-temperature conditions.

3.3. *Coherent vortical structures*

A fundamental and important issue in the analysis of coherent vortical structures is about how to define the vortex and its topological structure. Following the topological definition proposed by Chong et al. [31], Zhou et al. [32] used the iso-surface of the imaginary part of the eigenvalue of velocity gradient tensor to visualise vortices. This approach eliminates the region with vorticity but no local spiralling motion. Further, Pirozzoli et al. [15] employed the anisotropic velocity gradient tensor $A^*_{ij} = \partial u_i/\partial x_j - \vartheta/3\delta_{ij}$ to identify the vortex, where ϑ is the dilatation $\partial u_i/\partial x_i$. Then, a vortex is identified as the local region where $\boldsymbol{A}^*$ has one real eigenvalue (λ_r) and two complex conjugate ones ($\lambda_c^{\pm} = \lambda_{cr} \pm \mathbf{i}\lambda_{ci}$). The eigendirection associated with λ_r is represented as $\hat{\boldsymbol{v}}_r$, and the eigendirection associated with $\lambda_c^{\pm}$ as $\hat{\boldsymbol{v}}_c^{\pm} = \hat{\boldsymbol{v}}_{cr} \pm \mathbf{i}\hat{\boldsymbol{v}}_{ci}$. The imaginary part of the eigenvalue $\lambda_c^{\pm}$ is referred to as the local swirling strength of the vortex [32].

The three-dimensional instantaneous vortical structures educed by swirling strength criterion is exhibited in Figure 12 for the adiabatic condition. It is observed that the boundary layer is populated by symmetric hairpin-like and asymmetric hairpin-like (or cane-like) structures attached to the wall [33]. Once the vortical structures are educed, the orientation of the vortices needs to be quantitatively determined. The criteria of vortex orientation were examined systematically and summarised by Pirozzoli et al. [15] based on the DNS data of compressible turbulent boundary layer at $M_\delta = 2$. They found that three typical

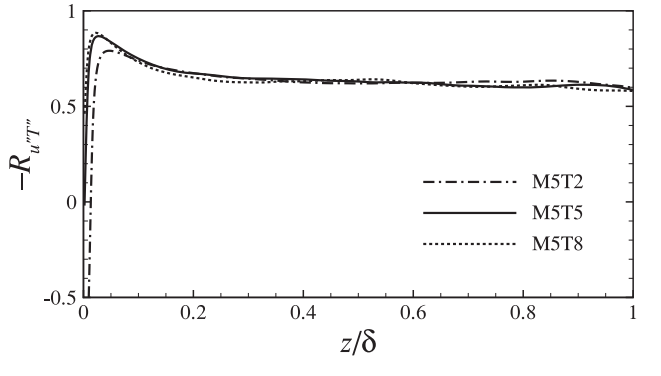

Figure 11. Plot of $-R_{u''T''}$ for different wall-temperature cases.

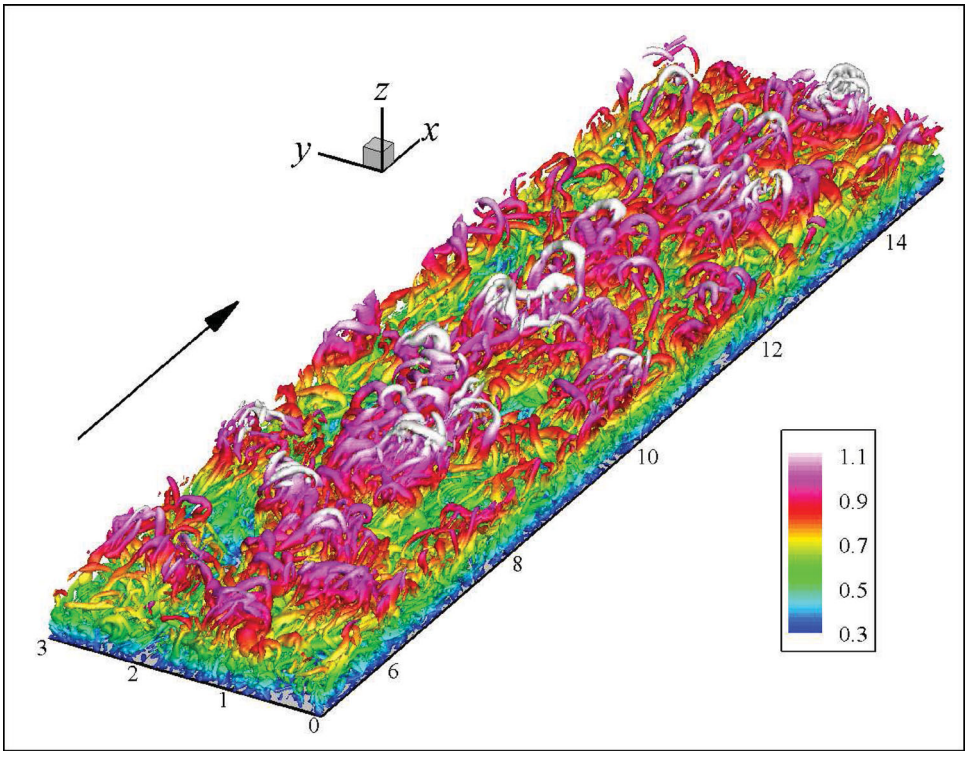

Figure 12. Instantaneous vortical structures educed by iso-surface of swirling strength ($\lambda_{ci} = 2c_\delta/\delta_0$) and coloured by z/δ_0 for the adiabatic condition (M5T5).

criteria, including local vorticity vector (i.e. $\boldsymbol{\omega}$-criterion), swirling plane normal direction (i.e. $\hat{\boldsymbol{v}}_c$-criterion, where $\hat{\boldsymbol{v}}_c = \hat{\boldsymbol{v}}_{cr} \times \hat{\boldsymbol{v}}_{ci}$), and local strain direction (i.e. $\hat{\boldsymbol{v}}_r$-criterion), are nearly equivalent for vortex orientation in the outer layer, and exhibit some differences in the inner layer. Actually, a universally accepted criterion of vortex orientation, in particular for sheet-like structures which are also important in supersonic boundary layers, has not been given; therefore, the determination of vortex orientation is still an issue.

3.3.1. *Orientation*

Here, we study systematically the $\boldsymbol{\omega}$-, $\hat{\boldsymbol{v}}_c$-, and $\hat{\boldsymbol{v}}_r$-criteria for vortex orientation in the inner and outer layers of compressible turbulent boundary layers. First, the preferred orientation of vorticity filaments is investigated using statistical analysis of the covariance of two vorticity components, which is defined as [12]

$$\overline{\omega_i \omega_j} = \int \int \omega_i \omega_j P(\omega_i, \omega_j) d\omega_i d\omega_j, \tag{11}$$

where $P(\omega_i, \omega_j)$ is the joint PDF of ω_i and ω_j. The integral of the covariance integrand $\omega_i \omega_j P(\omega_i, \omega_j)$ represents the contribution of the particular simultaneous combination of sign and magnitude of ω_i and ω_j to the vorticity covariance $\overline{\omega_i \omega_j}$ [12].

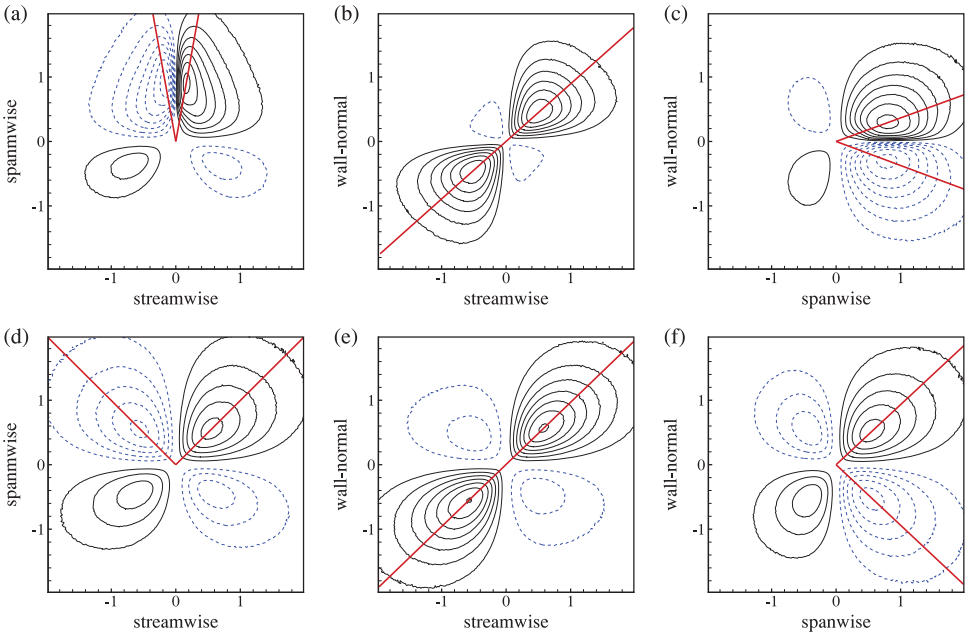

Figure 13. Covariance integrands of (a,d) streamwise and spanwise, (b,e) streamwise and wall-normal, and (c,f) spanwise and wall-normal components of $\omega/\langle\omega^2\rangle^{1/2}$ in the (a–c) inner layer and (d–f) outer layer the adiabatic condition (M5T5). The contour increment is 0.01 and outer contours are one increment above zero. Solid contour lines are positive and dashed contour lines are negative. The red line passes through the origin and the peak in the contours.

The covariance integrands of vorticity components for the adiabatic condition are shown in Figure 13, where the vorticity components are normalised by $\langle\omega^2\rangle^{1/2}$. The projection of vorticity filaments on the streamwise–spanwise (or x–y) plane in the inner layer ($z^+ < 40$) is given in Figure 13(a). The covariance integrand contour indicates that the dominance of the contributions comes from the first quadrant (Q_1) and the second quadrant (Q_2). In statistical sense, the orientation of segments of vorticity filaments with projection on the streamwise–spanwise plane making angles with the positive x-axis of $\alpha \equiv \arctan(\omega_y/\omega_x)$ can be inferred from the peaks with positive or negative value in these covariance integrand Q_1 and Q_2 quadrants, as represented by red solid lines. These vorticity filament segments, with angles of about $\alpha = 80^\circ$ and 100°, have the largest contribution to the $\overline{\omega_x\omega_y}$ covariance. This behaviour indicates that these vorticity filaments are oriented primarily in the positive spanwise direction in the inner layer. However, as shown in Figure 13(c) for the outer layer ($z^+ > 40$) in the Q_1, the angle decreases to about 45°, indicating that the vorticity filaments rotate toward the streamwise direction with increasing distance from the wall.

From the covariance integrands in the streamwise–wall-normal (or x–z) plane shown in Figure 13(b) and 13(e), it is seen that the dominance of the contributions occurs in the Q_1 and the third quadrant Q_3. According to the major contributions, the angles $\beta \equiv \arctan(\omega_z/\omega_x)$ of vorticity filaments with respect to the positive x-axis are 42° and -138° in the inner layer, and 44° and -136° in the outer layer. These characters are essentially consistent with the results of Wang and Lu [16] in the buffer layer and logarithmic layer for compressible turbulent boundary layer at $M_\delta = 2$.

Table 3. Vortex core orientation based on different criteria for M5T5.

	$z^+ < 40$				$z^+ > 40$			
	α	β	φ	$\hat{\varphi}$	α	β	φ	$\hat{\varphi}$
ω	80°	42°	20°	9°	45°	44°	43°	44°
$\lambda_{ci}\hat{\omega}$	79°	43°	25°	10°	46°	44°	44°	43°
$\lambda_{ci}\hat{v}_c$	77°	71°	54°	34°	50°	49°	46°	44°
$\lambda_{ci}\hat{v}_r$	28°	16°	27°	28°	44°	42°	42°	43°

As referred from Figure 13(c) and 13(f), the largest contribution to the covariance $\overline{\omega_y\omega_z}$ comes from the Q_1 and the fourth quadrant Q_4. On the streamwise–wall-normal plane, the angles $\varphi \equiv \arctan(\omega_z/\omega_y)$ of vorticity filaments with respect to the positive y-axis are $\pm 20°$ in the inner layer and $\pm 43°$ in the outer layer. It is indicated that the vorticity filaments rotate toward the wall-normal direction with increasing distance from the wall, which is consistent with experimental findings for the incompressible turbulent boundary layer [12].

However, it is commonly accepted that the near-wall boundary layer is populated by quasi-streamwise vortices with small inclination with respect to the wall plane. This behaviour indicates that coherent vortical structures are oriented primarily in the streamwise direction in the inner layer, which is in conflict with the results obtained by means of the covariance integrand of vorticity components. Moreover, it is easy to verify that the following relationship among the projection angles α, β, and φ holds

$$\tan\varphi = \tan\beta/\tan\alpha. \tag{12}$$

Therefore, the projection angle $\hat{\varphi}$ can be inferred from α and β by

$$\hat{\varphi} = \tan^{-1}\left(\frac{\tan\beta}{\tan\alpha}\right). \tag{13}$$

Then, it is obtained that the values of $\hat{\varphi}$ are $\pm 9°$ and $\pm 44°$ in the inner and outer layers, respectively. The distinct different values between φ and $\hat{\varphi}$ in the inner layer indicate that the projection angles α, β, and φ are inconsistent. Correspondingly, the relevant issue is that the covariance integrand of vorticity components cannot reliably determine the orientation of coherent vortical structure in the inner layer of turbulent boundary layer. Therefore, we further analyse the behaviours related to vortex orientation in the inner layer.

As shown in Figure 14 for the covariance integrands in the inner layer of M5T5, the criteria of vortex orientation are examined systematically by means of the covariance integrand. The vector fields are constructed with the modulus λ_{ci} and the directions corresponding to the various vortex orientation criteria, including the direction of vorticity vector $\hat{\boldsymbol{\omega}}$, swirling plane normal direction $\hat{\boldsymbol{v}}_c$, and local strain direction $\hat{\boldsymbol{v}}_r$. It is found that the projection angles inferred using different criteria are distinctly different in the inner layer. However, these criteria are nearly equivalent for vortices in the outer layer, the results of the outer layer are shown in Figure 15 using $\lambda_{ci}\hat{\boldsymbol{v}}_r$. In statistical sense, coherent vortical structures are symmetrical with respect to the y-plane. Thus, Table 3 lists the projection angles of vortices in the Q_1 in the inner and outer layers according to several criteria. In comparison with φ and $\hat{\varphi}$, we learn that the local strain swirling ($\hat{\boldsymbol{v}}_r$-criterion) can reasonably predict

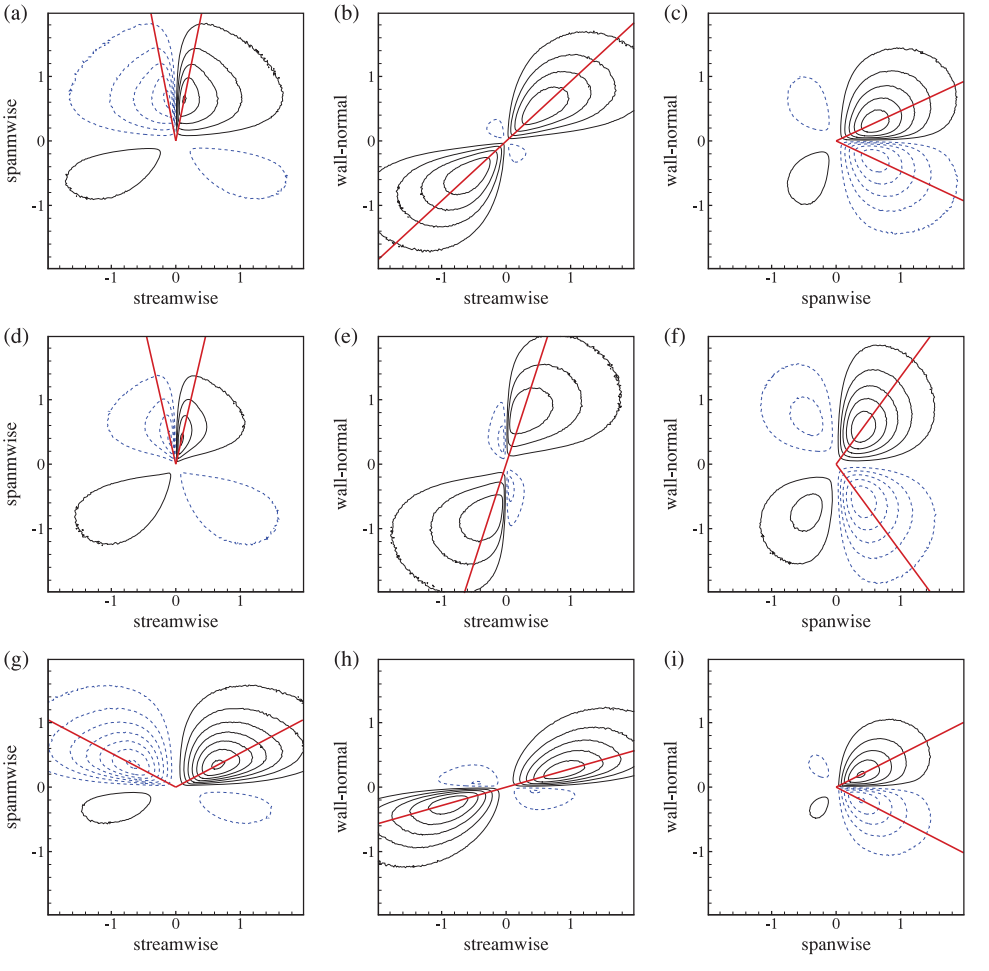

Figure 14. Covariance integrands in the inner layer for M5T5. (a–c) $\lambda_{ci}\hat{\omega}$, (d–f) $\lambda_{ci}\hat{v}_c$, and (g–i) $\lambda_{ci}\hat{v}_r$. All components are normalised by $\langle\lambda_{ci}^2|\Delta > 0\rangle^{1/2}$. For other details, see Figure 13.

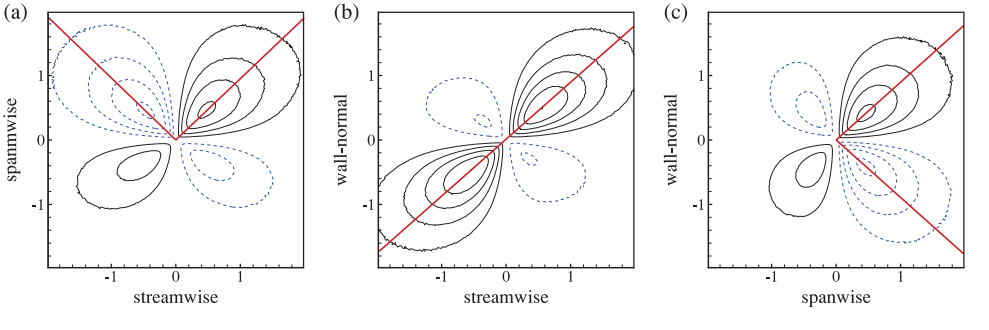

Figure 15. Covariance integrands of the components of $\lambda_{ci}\hat{v}_r$ in the outer layer for M5T5.

the projection angles in the inner and outer layers. Moreover, it is seen from Figure 14(g)–14(i) that the covariance integrand contours are consistent with the fact that the vortex structure tends to be a pair of counter-rotating quasi-streamwise vortices near the wall [9]. These demonstrate that the projection angles determined by the covariance integrand of the components of $\lambda_{ci}\hat{\boldsymbol{v}}_r$ describes reasonably the orientation of coherent vortical structures in statistical sense. In addition, Figure 14(b) and 14(e) shows that $\hat{\boldsymbol{\omega}}$- and $\hat{\boldsymbol{v}}_c$-criteria favour the directions normal to the wall. This is because of the presence of intense mean shear, but the tendency still persists even though the mean shear is subtracted [15].

It is seen from Figures 14(g) and 15(a) that the y-component of $\lambda_{ci}\hat{\boldsymbol{v}}_r$ of coherent vortical structures in statistical sense is positive, and the angles of vortical structures with respect to the positive y-axis on the x–y plane decrease from $\pm 62^\circ$ in the inner layer to $\pm 46^\circ$ in the outer layer. By comparing Figure 14(h) with Figure 15(b), it is found that the x-component of $\lambda_{ci}\hat{\boldsymbol{v}}_r$ decreases and the z-component increases with increasing distance from the wall. Viewed along the spanwise direction, the inclination angle of vortical structures with respect to the wall plane increases from 16° in the inner layer to 42° in the outer layer. The result of the outer layer compares favourably with previous findings, indicating that average vortices make an angle of 45° with respect to the wall [10,11]. As shown in Figures 14(i) and 15(c), the angles of vortical structures with respect to the positive y-axis on the y–z plane increase from $\pm 27^\circ$ in the inner layer to $\pm 42^\circ$ in the outer layer.

3.3.2. *Effect of wall temperature*

To investigate the effect of wall temperature on coherent vortical structures, Figure 16 shows the covariance integrands of the components of the vector $\lambda_{ci}\hat{\boldsymbol{v}}_r$ in the inner layer for M5T2 and M5T8. From Figures 14(g)–14(i) and 16, it is seen that, in the inner layer,

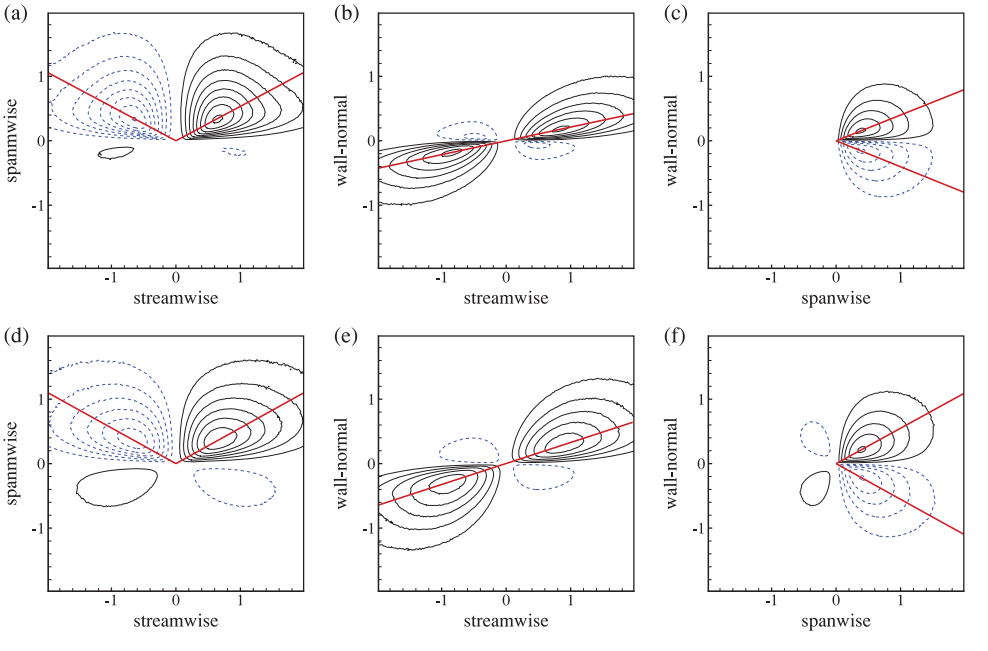

Figure 16. Covariance integrands of the components of $\lambda_{ci}\hat{v}_r$ in the inner layer for (a–c) M5T2 and (d–f) M5T8. For other details, see Figure 14.

Table 4. Vortex core orientation based on $\lambda_{ci}\hat{v}_r$ for different wall-temperature cases.

	$z^+ < 40$				$z^+ > 40$			
	α	β	φ	θ_e	α	β	φ	θ_e
M5T2	28°	12°	22°	11°	44°	41°	42°	32°
M5T5	28°	16°	27°	14°	44°	42°	42°	33°
M5T8	29°	18°	29°	16°	44°	42°	42°	33°

the z-component of $\lambda_{ci}\hat{\boldsymbol{v}}_r$ increases with the increase of wall temperature. This behaviour indicates that the local orientation of vortical structures of the inner layer favours the directions normal to the wall when the wall temperature increases. Moreover, in the outer layer, the covariance integrand contours of M5T2 and M5T8 (not shown here) are similar to M5T5 as shown in Figure 15.

Based on the analysis of the covariance integrands, the projection angles of vortical structures in the inner and outer layers are listed in Table 4. Due to the statistical symmetry of vortical structures, the results are only given in the covariance integrand Q_1 quadrant. The elevation angle (θ_e) of vortical structure, that is, the angle formed with the wall plane, is inferred from the projection angles by

$$\tan\theta_e = \frac{\tan\beta}{\left(\tan^2\alpha + 1\right)^{1/2}}. \tag{14}$$

The elevation angle of vortical structures is about 33° in the outer layer, consistent with the experimental result of incompressible turbulent boundary layer in the wake region [13]. However, the elevation angle of vortical structures in the inner layer increases from 11° to 16° with the increase of wall temperature.

To explain the effect of wall temperature on the orientation of coherent vortical structures, the mean swirling strength λ_{ci} in the swirling region ($\Delta > 0$) is shown in Figure 17 for different wall-temperature cases. It is noticed that the swirling strength of vortical structures

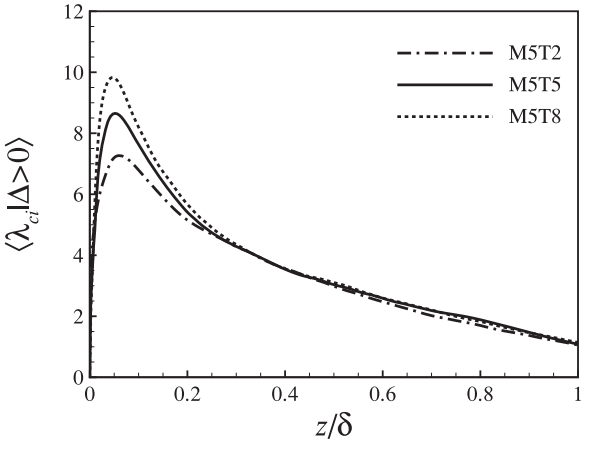

Figure 17. Conditional mean swirling strength as a function of the wall distance for different wall-temperature cases.

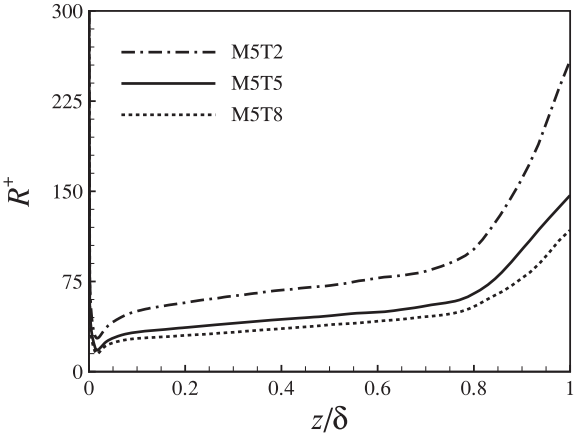

Figure 18. Distribution of mean radius of curvature of the vorticity field for different wall-temperature cases.

in the inner layer increases with the increase of wall temperature. Moreover, it is inferred from the decrease of the spanwise spacing of near-wall streaks [1,7] that the spanwise distance between the two legs of hairpin vortex decreases when the wall temperature increases. Therefore, the upward and backward velocities, induced by the head part of the hairpin vortex, increase with the increase of wall temperature in accordance to the Biot–Savart law. So, the self-induced motion results in further curl up of the hairpin vortex and the increase of the inclined angle with respect to the wall plane when the wall temperature increases.

As described by Zhou et al. [32], the self-induced motion in the neck region of the hairpin vortex is in the spanwise direction and it moves the two legs of hairpin vortex apart. The spanwise distance between the legs increases with increasing distance from the wall. Further, the geometrical features of vortical structures in the outer layer are quantitatively characterised by the statistics of the curvature of vortex lines, and then the local radius of curvature of a vortex line can be defined as [34]

$$R = \frac{\omega^3}{|\boldsymbol{\omega} \times (\nabla \boldsymbol{\omega} \cdot \boldsymbol{\omega})|}. \tag{15}$$

The distribution of the expected value of R shows a consistent increase with the distance from the wall in the outer layer. Moreover, the local radius of curvature R decreases in the increase of wall temperature, consistent with the effect of wall temperature on the spanwise distance of near-wall streaks. With the increase of R, the self-induced motion weakens and the interaction between hairpin vortices strengthens. Because of the relative dominance of the interaction over the self-induction in the outer layer, it is reasonably obtained that the orientation of vortical structures is nearly insensitive to the wall temperature.

4. Concluding remarks

Turbulent boundary layers at Mach 4.9 with the ratio of wall temperature to recovery temperature from 0.5 to 1.5 were investigated by means of DNS. The fundamental properties relevant to the influence of wall temperature on Morkovin's scaling, standard and modified

SRA relations, and coherent vortical structures were examined systematically and are summarised briefly as follows.

The van Driest transformed velocity profiles are examined and are essentially consistent with the incompressible linear scaling and logarithmic scaling lines, even though the logarithmic region is narrow due to low-Reynolds-number flows. The region of linear viscous sublayer shrinks with the decrease of wall temperature. This behaviour represents that the influence of wall temperature mainly occurs in the near-wall region. Based on the analysis of the mean temperature, it is obtained that a generalised form of the modified Crocco relation can be used to connect the mean temperature with the mean velocity for cool, adiabatic, and hot conditions. The effect of wall temperature on turbulence intensities and thermodynamic quantities fluctuations is also investigated. It is found that the scaling relations proposed for cool and adiabatic compressible turbulent boundary layers, such as Morkovin's scaling and modified SRA relations, are also applicable for hot condition.

The Reynolds analogies and the relevant properties are analysed for different wall-temperature conditions. The correlation between temperature and velocity fluctuations $R_{u''T''}$ and the turbulent Prandtl number Pr_t are insensitive to wall temperature and are approximately constant for most regions of boundary layer. When the wall temperature increases, the pressure fluctuation ($p'_{\mathrm{rms}}/\bar{p}_w$) decreases and the density ($\rho'_{\mathrm{rms}}/\bar{\rho}$) and temperature ($T'_{\mathrm{rms}}/\bar{T}$) fluctuations increase obviously. The relation between the density and temperature fluctuations under the second-order approximation, that is, Equation (6), is derived and verified to provide a reliable prediction. Moreover, the results obtained are mainly dependent on different wall-temperature conditions and are weakly associated with different Reynolds numbers considered in this study.

Based on the analysis of coherent vortical structures, it is found that the orientation of vortex core can be quantitatively determined by means of the vector with its direction and modulus using the local strain direction $\hat{\boldsymbol{v}}_r$ and the imaginary part of the eigenvalue of velocity gradient tensor λ_{ci}, respectively. With the increase of wall temperature, the spanwise distance between the two legs of the hairpin vortex increases and the mean swirling strength increases in the inner layer, thus the angle of vortical structures with respect to the wall plane increases. Moreover, with the increase in the local radius of curvature of vortical structures along the wall-normal direction, the interaction between hairpin vortices strengthens and dictates the dynamics of vortical structures. Therefore, the orientation of vortical structures is nearly insensitive to the wall temperature in the outer layer.

Acknowledgments

This work was supported by the National Natural Science Foundation of China (grant number 11132010), (grant number11072236) and the 111 Project (grant number B07033).

References

L. Duan, I. Beekman, and M.P. Martín, *Direct numerical simulation of hypersonic turbulent boundary layers. Part 2. Effect of wall temperature*, J. Fluid Mech. 655 (2010), pp. 419–445.

M. Morkovin, *Effects of compressibility on turbulent flows*, In: A. Favre (Ed.): *Mèchanique de la Turbulence*, Centre National de al Techerche Scientific, Paris, 1962, pp. 367–380.

H.H. Fernholz and P.J. Finley, *A critical commentary on mean flow data for two-dimensional compressible turbulent boundary layers*, Tech. Rep. 253, AGARD, France, 1980.

S.E. Guarini, R.D. Moser, K. Shariff, and A. Wray, *Direct numerical simulation of a supersonic boundary layer at Mach 2.5*, J. Fluid Mech. 414 (2000), pp. 1–33.

S. Pirozzoli, F. Grasso, and T.B. Gatski, *Direct numerical simulation and analysis of a spatially evolving supersonic turbulent boundary layer at $M = 2.25$*, Phys. Fluids 16 (2004), pp. 530–545.
L. Duan, I. Beekman, and M.P. Martín, *Direct numerical simulation of hypersonic turbulent boundary layers. Part 3. Effect of Mach number*, J. Fluid Mech. 672 (2011), pp. 245–267.
M. Lagha, J. Kim, J.D. Eldredge, and X. Zhong, *A numerical study of compressible turbulent boundary layers*, Phys. Fluids 23 (2011a), p. 015106.
L. Duan and M.P. Martín, *Direct numerical simulation of hypersonic turbulent boundary layers. Part 4. Effect of high enthalpy*, J. Fluid Mech. 684 (2011), pp. 25–59.
S.K. Robinson, *Coherent motions in the turbulent boundary layer*, Annu. Rev. Fluid Mech. 23 (1991), pp. 601–639.
T. Theodorsen, *Mechanism of turbulence*, Proceedings of the Second Midwestern Conference on Fluid Mechanics, Columbus, Ohio, 1952, pp. 17–19.
M. Head and P. Bandyopadhyay, *New aspects of turbulent boundary-layer structure*, J. Fluid Mech. 107 (1981), pp. 297–338.
L. Ong and J.M. Wallace, *Joint probability density analysis of the structure and dynamics of the vorticity field of a turbulent boundary layer*, J. Fluid Mech. 367 (1998), pp. 291–328.
B. Ganapathisubramani, E.K. Longmire, and I. Marusic, *Experimental investigation of vortex properties in a turbulent boundary layer*, Phys. Fluids 18 (2006), p. 055105.
E.F. Spina, A.J. Smits, and S.K. Robinson, *The physics of supersonic turbulent boundary layers*, Annu. Rev. Fluid Mech. 26 (1994), pp. 287–319.
S. Pirozzoli, M. Bernardini, and F. Grasso, *Characterization of coherent vortical structures in a supersonic turbulent boundary layer*, J. Fluid Mech. 613 (2008), pp. 205–231.
L. Wang and X.Y. Lu, *Statistical analysis of coherent vortical structures in a supersonic turbulent boundary layer*, Chinese Phys. Lett. 28 (2011), p. 034703.
G.S. Jiang and C.W. Shu, *Efficient implementation of weighted ENO schemes*, J. Comput. Phys. 126 (1996), pp. 202–228.
C.W. Shu and S. Osher, *Efficient implementation of essentially non-oscillatory shock-capturing schemes*, J. Comput. Phys. 77 (1988), pp. 439–471.
L. Wang and X.Y. Lu, *Flow topology in compressible turbulent boundary layer*, J. Fluid Mech. 703 (2012), pp. 255–278.
Y.B. Chu and X.Y. Lu, *Topological evolution in compressible turbulent boundary layers*, J. Fluid Mech. 733 (2013), pp. 414–438.
N.D. Sandham, Q. Li, and H.C. Yee, *Entropy splitting for high-order numerical simulation of compressible turbulence*, J. Comput. Phys. 178 (2002), pp. 307–322.
S. Pirozzoli, *Numerical methods for high-speed flows*, Annu. Rev. Fluid Mech. 43 (2011), pp. 163–194.
M.P. Martin, *Direct numerical simulation of hypersonic turbulent boundary layers. Part 1. Initialization and comparison with experiments*, J. Fluid Mech. 570 (2007), pp. 347–364.
S. Xu and M.P. Martin, *Assessment of inflow boundary conditions for compressible turbulent boundary layers*, Phys. Fluids 16 (2004), pp. 2623–2639.
N.A. Adams, *Direct numerical simulation of turbulent compression ramp flow*, Theor. Comput. Fluid Dyn. 12 (1998), pp. 109–129.
P. Bradshaw, *Compressible turbulent shear layers*, Annu. Rev. Fluid Mech. 9 (1977), pp. 33–54.
A. Walz, *Boundary Layers of Flow and Temperature*, MIT Press, Cambridge, Massachusetts, 1969.
P.G. Huang, G.N. Coleman, and P. Bradshaw, *Compressible turbulent channel flows: DNS results and modelling*, J. Fluid Mech. 305 (1995), pp. 185–218.
T. Maeder, N.A. Adams, and L. Kleiser, *Direct simulation of turbulent supersonic boundary layers by an extended temporal approach*, J. Fluid Mech. 429 (2001), pp. 187–216.
G.N. Coleman, J. Kim, and R.D. Moser, *A numerical study of turbulent supersonic isothermal-wall channel flow*, J. Fluid Mech. 305 (1995), pp. 159–183.
M.S. Chong, A.E. Perry, and B.J. Cantwell, *A general classification of three-dimensional flow fields*, Phys. Fluids A 2 (1990), pp. 765–777.
J. Zhou, R.J. Adrian, S. Balachandar, and T.M. Kendall, *Mechanisms for generating coherent packets of hairpin vortices in channel flow*, J. Fluid Mech. 387 (1999), pp. 353–396.
M. Stanislas, L. Perret, and J.M. Foucaut, *Vortical structures in the turbulent boundary layer: A possible route to a universal representation*, J. Fluid Mech. 602 (2008), pp. 327–382.
G. Farin, *Curves and Surfaces for Computer Aided Geometric Design*, Academic Press, Inc. Orlando, FL, USA, 1992.